Journal of Materials Chemistry C

ROYAL SOCIETY OF CHEMISTRY

PAPER

View Article Online
View Journal | View Issue

Cite this: J. Mater. Chem. C, 2022, 10, 5914

Spin to charge conversion in chemically deposited epitaxial $La_{0.9}MnO_3$ thin films capped with Pt†

Sergi Martin-Rio,[a] Alberto Pomar,[a] Carlos Frontera,[a] Hailin Wang,[a] Ramón Manzorro,[bc] César Magén,[bcd] Lluis Balcells,[a] Narcis Mestres[a] and Benjamin Martinez *[a]

Spin to charge conversion process in a broad range of temperatures is studied in $La_{0.92}MnO_3$/Pt bilayers prepared by polymer-assisted deposition (PAD). It is shown that an excellent LMO/Pt interface can be obtained in spite of using *ex situ* deposition of the Pt layer. The values obtained for the effective spin-mixing conductance, $g_{eff}^{\uparrow\downarrow} = 0.76 \times 10^{15}$ cm^{-2}, suggest that significant spin transport across the LMO/Pt interface could be achieved. Spin pumping experiments generate a transversal voltage signal V_{ISHE}, due to spin to charge conversion *via* inverse spin Hall effect, that has been detected down to about 100 K with values of the spin-Hall angle, θ_{SH}, of about 2.5%, slightly decreasing on reducing temperature in the analyzed temperature range. These results indicate that LMO is a promising perovskite building block for all-oxide multifunctional high-frequency spintronics devices and that PAD technique provides oxide epitaxial thin films of good quality adequate for spintronic applications.

Received 4th January 2022,
Accepted 14th March 2022

DOI: 10.1039/d2tc00048b

rsc.li/materials-c

Introduction

Complex oxides are a class of materials of great relevance because they offer a broad range of functionalities of strong technological interest. Nowadays, most of these applications require the use of thin films and heterostructures, thus boosting a strong activity in the field of thin film growth. Physical deposition methods, such as molecular beam epitaxy, RF sputtering and pulsed laser deposition, offer unquestionable advantages for the growth of metal oxide thin films like high epitaxial crystal quality, and precise control of composition and thickness at atomic scale.[1] However, these methods require high-vacuum and are expensive and difficult to scale up. In contrast, chemical deposition methods are easier to scale up and offer the possibility to grow over large areas at low cost while allowing an easy tuning of the stoichiometry.[2] In particular, polymer assisted deposition (PAD) has appeared as a competitive route for environmentally friendly approaches as it is based on the deposition of cationic aqueous solutions.[3] However, there exist some concerns regarding the suitability of films prepared by chemical methods for challenging applications requiring high microstructural quality and sharp interfaces, *e.g.* spintronics. Since the energy balance involved during the growth process is quite delicate, chemical growth methods may lead to a defect landscape different from that generated by using vacuum techniques, resulting in the modification of the physical properties of the films. Thus, relevant parameters for the development of spintronics devices, such as magnetic damping, α, magnetic anisotropy or spin-mixing conductance, $g^{\uparrow\downarrow}$, may be substantially different from that observed in thin films and heterostructures prepared by physical deposition methods.[4] On the other hand, the particular growth conditions of PAD, close to thermodynamic equilibrium conditions, have revealed to be very appropriate for the epitaxial growth of ternary and complex oxides thin films of a broad variety of materials.[4–6] In our previous work,[7] we showed that thin films of the ferromagnetic-metallic $La_{0.92}MnO_3$ (LMO) compound prepared by PAD exhibit magnetic damping values, α_{LMO}, of the order of 1×10^{-2}, similar to damping values reported for other perovskite oxide films prepared by physical methods.[8–10] Additionally, it was also observed that magnetic damping substantially increased in LMO films caped with Pt, $\alpha_{LMO/Pt} \approx 2.5 \times 10^{-2}$, thus suggesting a transfer of spin momentum from the LMO to the Pt layer by spin pumping (SP). These results allow envisaging that LMO films grown by PAD may potentially be an efficient spin source system in heterostructures for spintronic devices.

[a] Instituto de Ciencia de Materiales de Barcelona (ICMAB), CSIC, Spain. E-mail: ben.martinez@icmab.es
[b] Instituto de Nanociencia y Materiales de Aragón (INMA), CSIC-U. de Zaragoza, 50009 Zaragoza, Spain
[c] Laboratorio de Microscopías Avanzadas, U. de Zaragoza, 50018 Zaragoza, Spain
[d] Departamento de Física de la Materia Condensada, U. de Zaragoza, 50009 Zaragoza, Spain

† Electronic supplementary information (ESI) available: Compositional analysis of the LMO/Pt interface, details about the sample holder connections and analysis of the difrent factors contributing to the temperature dependence of VISHE. See DOI: 10.1039/d2tc00048b

The generation and transmission of spin currents necessary for the development of spintronics devices requires of low magnetic damping materials.[11] Previous results show that the spin pumping efficiency is significantly influenced by the damping constant.[10] Low magnetic damping constants may be achieved in transition metal oxide films, either in insulating materials as yttrium iron garnet or in half-metallic compounds, as the double exchange $La_{2/3}Sr_{1/3}MnO_3$.[12,13] However, in the latter case magnetic damping may be substantially increased due to extrinsic contribution associated with the scattering of conduction electrons by the two magnon scattering mechanism.[14] Additionally, surface/interface roughness and/or magnetic inhomogeneities originated from the defect landscape of the film may also increase extrinsic damping. Previous results regarding the generation of pure spin currents by SP in complex oxides, such as $SrIrO_3$, $SrRuO_3$ and double exchange manganites,[10,15–18] anticipate a major role of these materials in the development of the next generation of spin devices based on spin–orbit torques.[19] Therefore, it is of strong interest to clarify if complex oxide thin films prepared by chemical deposition methods are good enough for the generation and manipulation of pure spin currents. To analyze this possibility, we have chosen the $La_{0.92}MnO_3$ (LMO) compound. Bulk stoichiometric $LaMnO_3$ is a Mott insulator and an A-type antiferromagnet (AF), however it may become a ferromagnet (FM) in thin film form, due to structural strain,[20] or by introducing cationic vacancies (in both La or Mn sites).[21] La vacancies promotes de appearance of a Mn^{3+}–Mn^{4+} mixed valence state to maintain charge neutrality and a double exchange mediated FM and metallic state is generated.[21] With 8% of La vacancies LMO thin films prepared by PAD exhibit a robust ferromagnetic ordering with a FM transition temperature above room temperature ($T_C \approx 320$ K), slightly below that of ideally doped $La_{1-x}Sr_xMnO_3$ perovskites, but with a smaller cationic disorder and larger conductivity values, making it interesting for spintronic applications. In this work we have studied the spin injection and spin-charge conversion processes in LMO/Pt bilayers by using a broadband ferromagnetic resonance spectrometer for SP. Inverse spin Hall effect (ISHE) voltage signals were measured in a broad range of temperatures, in spite of larger values of magnetic damping, making evident that LMO films prepared by PAD are of high quality, overcoming the challenging difficulties of surface roughness and homogeneity control, even for properties highly dependent on defect structure as magnetic damping and spin currents generation and transmission.

Experimental

Epitaxial LMO thin films were grown on (001)-STO substrates *via* PAD.[3,7] Individual solutions of La^{3+} and Mn^{2+} were prepared by dissolving $La(NO_3)_3{\cdot}6H_2O$ and $Mn(NO_3)_2{\cdot}5H_2O$ in water with ethylenediaminetetraacetic acid (EDTA) in a 1 : 1 molar ratio. Polyethylenimine (PEI), Sigma Aldrich Ref. 408727, with an average molecular weight of 25 000 was then added to each solution in a 1 : 1 mass ratio to EDTA. The cations bind to PEI through an electrostatic EDTA–PEI interaction.[3] This feature not only ensures an even distribution of metal cations in the solution, but also serves to adjust the viscosity of the solution. The individual solutions were filtered using an Amicon filtration unit (10 kDa), and retained portions were analyzed by inductively couple plasma (ICP; Optima 4300 DV ICP.OES Perkin-Elmer). Finally, the solutions were mixed according to the desired final stoichiometry, La : Mn 0.92 : 1. Typical solution viscosity values were in the range $\eta \approx 3$–4 mPa s (measured with a DMA 4100 M Anton Paar densimeter, with a microviscometer module Lovis 2000ME). The precursor solutions obtained in this way were spin-coated (4000 rpm, for 90 seconds) on 0.5 × 0.5 cm^2 (001)-STO substrates from Crystec GmbH, Germany. Prior to deposition, the as-received STO substrates were chemically etched and thermally treated to generate TiO_2-terminated surfaces with atomically flat terraces.[22] Finally spin coated films were annealed for the elimination of the organic component at low temperatures ($\approx$500 °C), and phase formation and crystallization at higher temperatures, under oxygen flow to avoid the formation of oxygen vacancies. Thermal annealing was performed using a horizontal tube furnace at 980 °C for 30 min, and oxygen flow above 0.2 L min^{-1}. Consequently, mirror-like films that cover the whole surface of the substrate, and exhibit a low surface roughness (RMS values below ~ 1 nm) were obtained (see Fig. 1). In this way LMO samples of thickness, $t \approx 17$ nm, as determined by X-ray reflectometry, prepared using solutions with a total cation concentration of 240 mM were fabricated. Systematic θ–2θ scans in X-ray measurements showed that only the (00l) reflections of the film and substrate are present indicating the excellent purity of the phase and the optimum c-axis alignment of the grown films.[7] The excess of material at the edges and corners of the sample have been removed by acid treatment (see ref. 7 for details). Previously to the acid treatment, a circular pattern, made by means of optical lithography, has been imprinted on the sample in order to control the total volume of the magnetic film. The overall result is a circular $La_{0.92}MnO_3$ thin film with a diameter of 4.4 mm and no excess of material at the corners nor the edges. Then, samples were capped with a Pt layer deposited at room temperature, in Ar–H_2

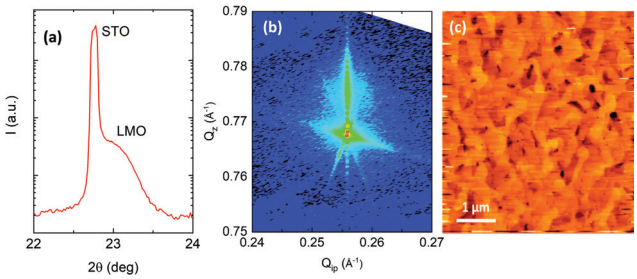

Fig. 1 (a) θ–2θ scan around the (001) STO reflection. (b) Reciprocal space map in the vicinity of the ($\bar{1}03$) STO peak revealing in-plane compressive strain in the films. Pseudocubic notation is always used. (c) Topography of the surface of an LMO thin film obtained *via* AFM in tapping mode. Overall roughness rms ≈ 1 nm.

atmosphere and working pressure of 5 mTorr, using a dc magnetron sputtering. Prior to Pt deposition, LMO film's surface was cleaned using a combination of acetone and ethanol and further anneal up to 500 °C for 1 min. The estimated thickness of Pt layer is about 6 nm. Additionally, the structural characterization of both the LMO surface and its interface with the STO substrate has been studied by a combination of atomic force microscopy (AFM), X-rays and scanning transmission electron microscopy (STEM) methods. Aberration corrected STEM characterization was carried out in a probe-corrected FEI Titan 60–300 operated at 300 kV, and equipped with a high-brightness field emission gun (X-FEG), a CETCOR aberration corrector for the probe from CEOS, and a Tridiem GIF spectrometer 866 ERS from Gatan. Atomically resolved images with Z contrast were acquired by high-angle annular dark field (HAADF); the convergence semiangle of the probe was 24 mrad to yield a probe size < 1 Å. STEM spectrum imaging was performed by combining HAADF imaging with Electron Energy Loss Spectroscopy (EELS) with a beam current of $\sim$180 pA, an energy dispersion of 0.1 eV, and a collection semiangle of about 45 mrad. EELS spectra were collected with an exposure time of 0.5 s, and afterwards noise-filtered by Principal Component Analysis (PCA).[23]

Results and discussion

θ–2θ scan around the (001) diffraction peak is presented in Fig. 1a. Fitting of the (00l) peak positions leads to a pseudocubic out-of-plane parameter of $a_{\perp} \approx 3.87$ Å. Moreover, the strain state of the LMO film was studied by using reciprocal space maps around $(\bar{1}03)_{STO}$ reflection, as shown in Fig. 1b. The fact that both peaks lie on the same Q_{ip} coordinate line indicates that the LMO film is fully strained. Therefore, the in-plane lattice parameter of the LMO film, $a_{||}$, matches that of the substrate one, *i.e.*, $a_{||} = 3.905$ Å, resulting in a pseudocubic cell volume of $V_{pc} \sim 59.3$ Å^3.[7] Surface topography of the as-grown LMO sample is shown in Fig. 1c. A relatively flat surface with an RMS roughness of about 1 nm is observed.

The quality of the LMO/Pt bilayers has been analyzed by using STEM. LMO film is epitaxial and shows and excellent crystalline quality without defects while Pt is of polycrystalline nature. No structural modifications are observed at the LMO/Pt interface (see Fig. 2a). A chemical analysis close to the LMO/Pt interface has been performed by Electron Energy Loss Spectroscopy (EELS) (see Fig. 2b and Fig. S1 and S2, ESI†). The Mn–$L_{2,3}$ edge shows a uniform fine structure when monitored deep into the LMO film, while the L_3 line experiences a gradual shift of $\sim$0.8 eV to lower energy at the interface, in the last 2–3 unit cells of LMO below Pt. This redshift indicates qualitatively a higher abundance of Mn^{3+}, thus a Mn reduction at an interface with lower oxygen content than the inner part of the LMO film.[24]

The static magnetic properties of the LMO films were studied using a SQUID magnetometer by Quantum Design. The diamagnetic contribution of the substrate and other instrumental contributions for DC magnetization measurement were properly corrected.[25] The possible relative error when determining the saturation magnetization (M_s) by SQUID measurements was estimated to be approximately 5% and is mainly ascribed to the error in the determination of the actual volume of the samples. The saturation magnetization value obtained at low temperatures for the LMO film is around 550 emu cm^{-3}, in excellent agreement with the theoretical value for $La_{0.92}MnO_3$ ($\approx$568 emu cm^{-3}). The magnetization *versus* temperature, M(T), curves of the LMO film before and after the Pt deposition are depicted in Fig. 3a. As it can be observed, the Curie tem temperature in both cases is almost the same (around 320 K). However, the absolute value of the saturation magnetization after the Pt deposition is slightly reduced ($\sim$9%) with respect to the saturation value of the LMO film alone. This small reduction may be attributed to minute changes of the oxygen content, as shown by EELS spectra (see Fig. 2 and Fig. S1, ESI†), during the deposition of the Pt capping layer in a slightly reducing atmosphere to prevent oxidation. On the other hand, in Fig. 3b, the hysteresis loops ($M(H)$ curves) at different temperatures of the LMO/Pt bilayer show that the coercive field increases with decreasing temperature. An important feature of $M(T)$ and $M(H)$ curves is the lack of any signal of secondary magnetic phases or magnetic inhomogeneities in the samples.

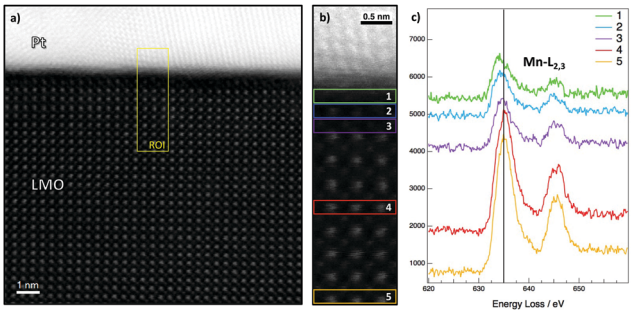

Fig. 2 (a) Atomic resolution HAADF-STEM image of the LMO/Pt interface. (b) HAADF signal of the interface region marked with a yellow rectangle in b, where EELS experiment was performed. (c) Background-subtracted EELS spectra of the Mn–$L_{2,3}$ edge after noise reduction, integrated along the regions indicated in (b).

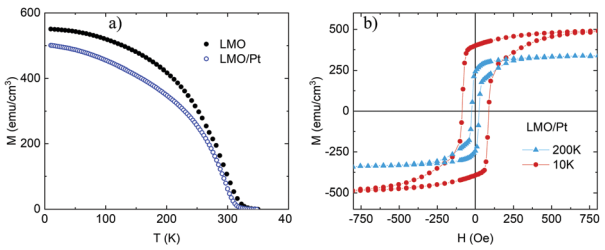

Fig. 3 (a) Temperature dependence of the magnetization for the LMO film before and after deposition of the Pt capping layer. A decrease in the magnetization after the Pt deposition can be appreciated. The magnitude of the applied, in-plane, magnetic field is 1 kOe. (b) Hysteresis loops of the LMO/Pt bilayer, with the external applied field parallel to de sample plane, for different temperatures.

The dynamic magnetic properties of the LMO and LMO/Pt thin films were studied by means of ferromagnetic resonance spectroscopy (FMR) using a commercial broadband coplanar waveguide (CPW) (by NanOsc) inserted into a Physical Properties Measurement System (PPMS by Quantum Design). The transversal voltage signal generated by ISHE in the LMO/Pt bilayer system has been measured by using a 2128A Keithley nanovoltmeter. This equipment has been programmed to act synchronously with the FMR spectrometer in order to measure both the FMR spectral curves and ISHE voltage signal simultaneously. A custom-made CPW specifically designed to measure voltage signals in FMR experiments has been employed. The electrical contact with the sample is enabled through two parallel Au ribbons on both sides of the CPW with bumps raised 20 μm above the sample holder surface. An image of the actual experimental setup is shown in the ESI† (see Fig. S3, ESI†). Each measurement was performed at a fixed temperature and sweeping the externally applied magnetic field, H, for several fixed microwave frequencies (from 2 GHz to 16 GHz). The external static magnetic field was applied in-plane and parallel to the [100] substrate direction. An example of the FMR absorption spectrum obtained at T = 200 K for the LMO film and LMO/Pt bilayer is shown in Fig. 4a. As evidenced by the figure the presence of a Pt capping layer promotes an enhancement of the resonant absorption line-width.

The derivative of the FMR spectra is described as the sum of symmetric and antisymmetric Lorentzian derivative contributions, *i.e.*,

$$\frac{\mathrm{d}s}{\mathrm{d}H} \propto \frac{\mathrm{d}}{\mathrm{d}H}\left\{\frac{\Delta H^2}{\Delta H^2 + 4(H - H_{\mathrm{res}})^2} + \frac{\Delta H \cdot (H - H_{\mathrm{res}})}{\Delta H^2 + 4(H - H_{\mathrm{res}})^2}\right\} \quad (1)$$

By fitting the FMR absorption spectrum at each microwave frequency using eqn (1) both the resonance field (H_{res}) and line width (ΔH) can be determined. The frequency dependence on the resonance field is conditioned by the existence of in-plane anisotropy in these films, as shown in our previous report.[7] Therefore, for the [100] substrate direction, it may be written as:[26]

$$f = \frac{\gamma}{2\pi}\mu_0\left(H_{\mathrm{res}} + H_{4\mathrm{ip}}\right)^{1/2} \times \left(H_{\mathrm{res}} + M_{\mathrm{eff}} + H_{4\mathrm{ip}}\right)^{1/2} \quad (2)$$

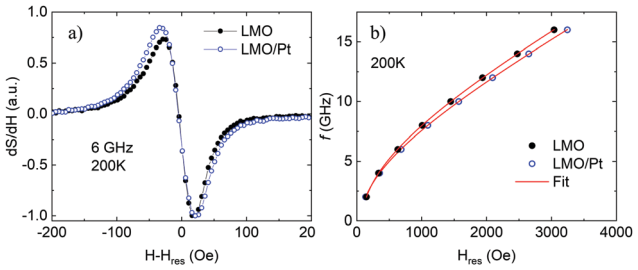

Fig. 4 (a) Example of the derivative of the resonant absorption line measured at T = 200 K and at a frequency of 6 GHz. The increase of the line-width after Pt capping is evidenced. (b) Kittel curves for the LMO and LMO/Pt systems showing the shift in the resonance field at high frequencies. The fitting curves (red lines) have been obtained using eqn (2).

being $\gamma = \mu_{\mathrm{B}}g/\hbar$ the gyromagnetic ratio, $H_{4\mathrm{ip}} = +2K_{4\mathrm{ip}}/M_{\mathrm{s}}$ a four-fold in-plane anisotropy field, and M_{eff} the effective magnetization, which is defined as $4\pi M_{\mathrm{eff}} = 4\pi M_{\mathrm{s}} - 2K_{\perp}/M_{\mathrm{s}}$ and includes the out-of-plane uniaxial anisotropy term $K_{\perp}$. Moreover, the resonance linewidth ΔH, which quantifies the magnetic relaxation processes in the system, depends linearly on the frequency, being the magnetic damping the slope of the line, *i.e.*,

$$\Delta H = \Delta H(0) + \frac{4\pi\alpha}{\gamma}f \quad (3)$$

where $\Delta H(0)$ is the so-called inhomogeneous line broadening or damping, which represents the relaxation processes due to extrinsic contributions such as magnetic inhomogeneity in the sample, and α is the Gilbert damping parameter, which generally quantifies the intrinsic damping contribution to the overall magnetic relaxation processes. This parameter, however, may include extrinsic contributions such as two-magnon scattering and SP. An example of the dependence of H_{res} on the measuring frequency for both LMO and LMO/Pt is shown in Fig. 4b together with the fit using eqn (2). The observed shift to higher resonance fields for LMO/Pt sample reflects the small decrease of the saturation magnetization, as already found in SQUID measurements. Worth to mention here that, during the fitting process, γ and M_{eff} are closely correlated (see eqn (2)) and different values might result in equally good fittings. Nevertheless, coincidences of the values of the obtained gyromagnetic ratio and the saturation magnetization changes, in accordance with the $M(T)$ measurement, in both systems give further support to the goodness of this fit. Therefore, using a mean γ value of 29.16 GHz T^{-1}, a g-factor of 2.08 is obtained, which is slightly higher than the spin-only value of 2 usually observed in manganites, suggesting a small contribution from the orbital angular momentum.[7]

On the other hand, the increase of the resonance linewidth, ΔH, in the LMO/Pt bilayer with respect to the LMO alone is also shown in Fig. 4a. As it has been stated previously, the resonance line width is related to magnetic relaxation processes in the system. Therefore, an increased line width would be related to additional dissipation channels in the LMO/Pt bilayer with respect to the LMO film. In fact, it could be indicative of the flow of spin angular momentum, *i.e.* SP effect, whereby the resonant precession of the LMO magnetization injects a pure spin current into the Pt film. As shown in our previous work,[7] values of the Gilbert damping parameter at T = 150 K are around 1×10^{-2} for LMO, and increase appreciably, to $\sim 2.5 \times 10^{-2}$, for LMO/Pt bilayers. These values are larger than these reported in similar high-quality complex oxide perovskites thin films grown by physical methods,[27,28] therefore it is of strong interest to verify the actual capability of PAD prepared LMO films to act as spin injectors. The efficiency of the spin injection across the LMO/Pt interface is described by the effective spin-mixing conductance, $g_{\mathrm{eff}}^{\uparrow\downarrow}$, which is the phenomenological parameter that quantifies the spin transparency of the magnetic/nonmagnetic (NM) layer systems interface. $g_{\mathrm{eff}}^{\uparrow\downarrow}$ of the LMO/Pt interface can be estimated from the change in the magnetic damping, *i.e.* $\Delta\alpha = \alpha_{\mathrm{LMO/Pt}} - \alpha_{\mathrm{LMO}}$, through the

relation $\Delta\alpha = (g\mu_B/4\pi M_s t_{LMO})g_{eff}^{\uparrow\downarrow}$, which results in an effective spin-mixing conductance $g_{eff}^{\uparrow\downarrow} = 0.76 \times 10^{15}$ cm^{-2}, that is similar to values reported for other perovskite oxide films[27,29] and slightly smaller than values reported for Py/Pt bilayers.[30,31] Since a large value of $g_{eff}^{\uparrow\downarrow}$ implies a large spin current, our results suggest that significant spin transport across the LMO/Pt interface could be achieved in spite of the *ex situ* deposition of Pt capping layer.

In order to assess the role of the chemical solution grown LMO films as effective spin injectors and verify that an actual injection of a pure spin current into the Pt layer takes place, the transversal voltage signal, due to spin to charge conversion through ISHE, across de Pt layer has been measured. In materials with large spin–orbit coupling, such as Pt, a pure spin current can be converted into a charge current, and *vice versa*, due to ISHE and spin Hall effect (SHE).[32] The effective detection of SP-induced ISHE voltage signal allows to circumvent the problem of interfacial spin decoherence with important implications in the quantification of crucial spintronic parameters such as the spin Hall angle or the spin diffusion length.[33–35]

In SP experiments, the line shape of the measured voltage signals follows that of the FMR spectra, *i.e.*, Lorentzian curve, therefore the measured voltage signal is given by the following expression:

$$V = \frac{V_s \Delta H^2}{\Delta H^2 + (H - H_{res})^2} + \frac{V_{as} \Delta H \cdot (H - H_{res})}{\Delta H^2 + (H - H_{res})^2} \qquad (4)$$

being V_s and V_{as} the symmetric and anti-symmetric voltage amplitudes of the overall signal line. It is worth mentioning that in most of SP-induced voltage measurements, besides ISHE, there may be contributions coming from the so-called spin rectification effects (SRE).[36] SRE arise from the synchronous coupling of the microwave magnetic field induced by the CPW and the time-varying magnetization of the FM sample in the form of magnetoresistance, which in overall result in a non-vanishing dc voltage signal. Nevertheless, since the resistivity of the LMO film is several orders of magnitude higher than that of Pt, SRE are expected to be negligible in our case.[7,37]

The experimental voltage signals at 200 K for the LMO/Pt bilayer are shown in Fig. 5. As it can be observed, the common trend of all the voltage curves is the dominance of the symmetric voltage amplitude, as expected for a voltage signal generated by ISHE (V_{ISHE}) free from parasitic SRE signals. The other important feature of the voltage curves is that they are all positive, in agreement with the expected polarity for an ISHE generated signal according to our experimental setup (see ESI†).

Fig. 5 also makes evident that the frequency dependence of voltage signal is not monotonic. In principle the spin current generated by SP is expected to be proportional to the precession frequency f,[38] and so does the ISHE voltage signal (V_{ISHE}), however, it is observed that the spin current slightly decreases with increasing frequency.[39] This behavior is generated due to the fact that even both, magnetization–precession and the spin

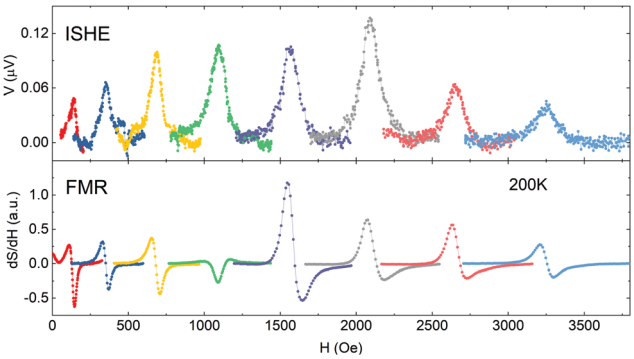

Fig. 5 Transverse voltage measurements for the LMO/Pt bilayer at different microwave frequencies (upper panel). The corresponding derivative of the FMR absorption line is shown in the bottom panel.

current generated by a cycle of the precession of magnetization, depend on frequency they have different frequency dependencies giving place to a sort of compensation effect. V_{ISHE} is proportional to the elliptical area of the magnetization precession trajectory, S, increasing the excitation frequency generates a reduction of the cone angle leading to a reduction of S roughly dependent on f^{-2}. Since V_{ISHE} is proportional to $f{\cdot}S$ a linear dependence on f^{-1} is roughly expected.[39,40]

From the values of the ISHE voltage signal, and assuming a $\lambda_S \approx 3$ nm (according to the resistivities of the Pt layer, namely $\rho \sim 40$ μΩ cm), a value of the Hall angle, $\theta_{SH} \sim 0.025 \pm 0.005$, slightly decreasing on reducing temperature in the analyzed temperature range, is derived. This value, in the range of low values reported in the literature, agrees well with previous reports for systems with similar values of Pt conductivity.[41]

On the other hand, the temperature dependence of V_{ISHE} is shown in Fig. 6. As expected, the intensity of the voltage signal decreases on approaching T_C since the magnetization of LMO layer decreases and so does the spin current injected into the Pt layer. However, it is also observed that the voltage signal decreases on cooling down the samples and becomes vanishing

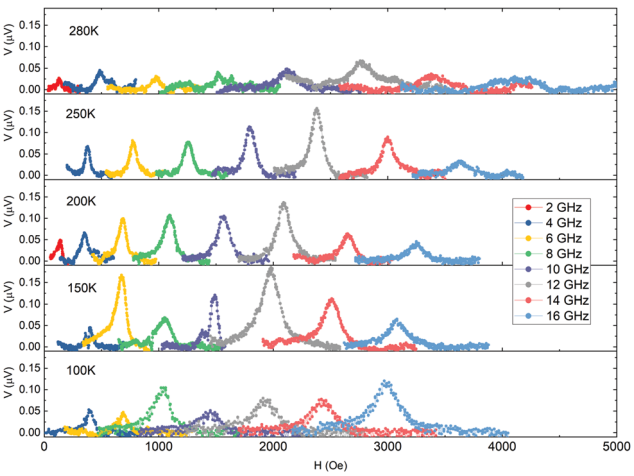

Fig. 6 Temperature dependence of the transverse voltage signal for the LMO/Pt bilayer at different frequencies.

small below 100 K when the magnetization of the LMO layer is already saturated.

Reports regarding the temperature dependence of V_{ISHE} are scarce and sometimes confusing. Temperature dependence of V_{ISHE} has been reported in $La_{0.7}Sr_{0.3}MnO_3/SrRuO_3$ (LSMO/SRO) bilayers showing the expected decrease on approaching T_C of LSMO.[42] However, the transition of SRO to the low temperature ferromagnetic phase at $T_C \sim 155$ K precludes the access to the low temperature behavior of V_{ISHE}. Temperature dependence of V_{ISHE} on LSMO/Pt bilayers has been reported by V. A. Atsarkin *et al.*[43] In this case it is shown that V_{ISHE} follows approximately the temperature dependence of the square of the magnetization of LSMO, decreasing on approaching T_C and showing a saturation effect below about 200 K. Unfortunately, experimental results are truncated at 100 K, so the behavior of V_{ISHE} at low temperature cannot be inferred. In order to clarify what the behavior at low temperatures should be, we have analyzed the expression of V_{ISHE} to try to derive the expected behavior of the different parameters appearing in the equation. According to the analysis in ref. 31 and after some algebra V_{ISHE} can be written as:[43]

$$V_{ISHE} = QR\lambda\theta_{SH}\tanh\left(\frac{t_{Pt}}{2\lambda}\right)p\Delta H^{-2}g_{eff}^{\uparrow\downarrow} \quad (5)$$

being Q a temperature-independent factor, R the total resistance of the measured section, λ the spin diffusion length in Pt, t_{Pt} the thickness of the Pt layer, ΔH half the resonance linewidth and p a factor that considers the effects of ellipticity of the spin precession in the FM film and demagnetizing fields. As pointed out in ref. 43, once the magnetization reaches the saturation value, the p factor is almost constant down to the low temperature regime (see Fig. S5 in ESI†). On the other hand, the change in resonance linewidth with temperature shows a non-monotonic behavior (see Fig. 7b). It initially decreases with decreasing temperature, but its behavior changes rapidly and begins to increase below about 200 K and the growth rate becomes noticeably more pronounced below 100 K. The temperature dependence of R exhibits a clear reduction on cooling down the sample since, both the Pt and the LMO layers have metallic behavior in this range of temperatures (see Fig. S5, ESI†). However, the spin Hall conductivity, σ_{SHE}, of Pt is found to be almost constant.[44] The temperature dependence of λ, θ_{SH} and $g_{eff}^{\uparrow\downarrow}$ is somehow more controversial. For instance, S. Meyer *et al.*[45] reported that in yttrium iron garnet/Pt hybrid structures θ_{SH} decreases almost to the half on cooling from room temperature to 10 K, wile λ and $g_{eff}^{\uparrow\downarrow}$ remain almost constant. However, this is in contrast to subsequent reports in Pt that point to an almost temperature-independent behavior of θ_{SH}.[46] In fact, we observed a smooth reduction of θ_{SH} on lowering temperature (see Fig. S4, ESI†). On the other hand, experimental results in LSMO/Pt bilayers show that $g_{eff}^{\uparrow\downarrow}$ is proportional to the square of the magnetization,[43] so that once saturation is reached it is basically independent of temperature. By contrast, λ exhibits a clear temperature dependence since it depends on the spin relaxation mechanism.[47] Some reports indicate that λ at Pt could be up to an order of magnitude higher at low temperature,[48] however as it depends on the spin relaxation mechanism could be sample-dependent. A simulation of the temperature dependence of V_{ISHE} can be obtained by introducing the temperature dependence of the different quantities included in eqn (5) (see Fig. S4 and S5 in ESI†). As shown in Fig. 7a the temperature dependence of the normalized V_{ISHE} is non-monotonic and exhibits a clear maximum at about 200 K, in rough agreement with the experimental observations. It is also worth mentioning that below 100 K V_{ISHE} signal is very small, as it is at high temperature close to T_C. Thus, this would explain why no V_{ISHE} signal is detected below 100 K. Interestingly, the variation of the FMR linewidth shown in Fig. 7b, exhibits just the complimentary behavior with a minimum around 200 K.

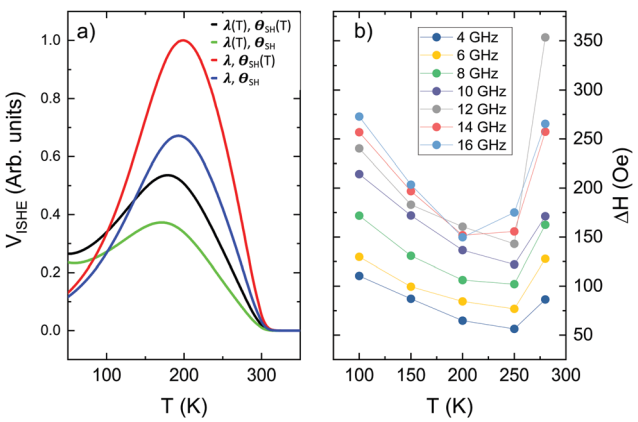

Fig. 7 (a) Simulation of the temperature dependence of the V_{ISHE} signal according to eqn (5) introducing the T-dependence of the different variables involved, *i.e.* λ, θ_{SH}, p, $g_{eff}^{\uparrow\downarrow}$, ΔH. (see Fig. S4 and S5 in ESI†). Data has been normalized by the value at maximum. Different scenarios have been considered for λ and θ_{SH}. Temperature-dependence, *i.e.* $\lambda(T)$, $\theta_{SH}(T)$ or no dependence in temperature at all, *i.e.* λ, θ_{SH}. (b) Measured temperature dependence of the FMR linewidth ΔH.

Taking into account the temperature dependence of the different variables involved in the eqn (5), *i.e.* λ, θ_{SH}, p, $g_{eff}^{\uparrow\downarrow}$, ΔH, it seems quite evident that the observed variation of V_{ISHE} is dominated by the temperature dependence of ΔH. Thus, we should conclude that the strong reduction of V_{ISHE} on lowering temperature is due to the increase of damping. In fact, a similar behavior has been observed in Pt/yttrium iron garnet bilayers in which a strong reduction of VISHE was detected on lowering temperature,[49] which was also attributed to a strong increase of damping on lowering temperature. At this point it is also important to remember that on lowering temperature extrinsic contributions to damping, such as two-magnon scattering, defects, changes of magnetic anisotropy, presence of interfaces, *etc.*, might substantially increase the damping, broadening resonance peaks, thus masking spin pumping effects and making it difficult to measure V_{ISHE} as the temperature drops below 100 K.[50,51] Moreover, very recent results in $La_{0.7}$ $Sr_{0.3}$ MnO_3 (LSMO),[52] a double exchange ferromagnet thus, with magnetic behavior very similar to that of our LMO samples, clearly exhibits a strong increase of damping on reducing temperature. The observed temperature dependence of damping is interpreted

considering two contributions, resistive-like and conductive-like, as in Kambersky's torque-correlation model[53] and an additional term due to spin pumping. This latter term is attributed to the appearance of an insulating and magnetically active dead layer, caused by the lowering of the double exchange mechanism at surface and interfaces. Since LMO has a very similar magnetic behavior to that of LSMO, and in both cases magnetic interactions are mediated by the double exchange mechanism, this additional term may also contribute to the enhancement of damping in our case.

Conclusions

In conclusion, in this paper we have analyzed spin to charge conversion processes in LMO/Pt bilayers, were the LMO epitaxial layer has been prepared by using PAD method in a broad range of temperatures. It is shown that PAD allows obtaining LMO films of excellent crystalline and surface quality. Additionally, it is also shown that an excellent LMO/Pt interface can be obtained using *ex situ* deposition of the Pt layer. Values of the Gilbert damping parameter are $\alpha \approx 1 \times 10^{-2}$ for LMO, and increase appreciably for LMO/Pt bilayers. These values are larger than those reported in similar high-quality complex oxide perovskites thin films grown by physical methods. However, the values obtained for the effective spin-mixing conductance, $g_{\mathrm{eff}}^{\uparrow\downarrow} = 0.76 \times 10^{15}$ cm^{-2}, are similar to values reported for other perovskite oxide films. Thus, our results suggest that significant spin transport across the PAD deposited LMO/Pt interface could be achieved in spite of the *ex situ* deposition of the Pt capping layer. Spin pumping experiments have been performed in a broad temperature range and a transversal voltage signal V_{ISHE}, due to spin to charge conversion, has been measured down to about 100 K. The high resistance of the LMO layer, compared to that of Pt layer, precludes the appearance of parasitic spin rectification effects and therefore V_{ISHE} signal is fully symmetric. V_{ISHE} exhibits a non-monotonic temperature dependence and becomes vanishing small below about 100 K. The strong reduction of V_{ISHE} on decreasing temperature is attributed to the increase of the magnetic damping. These results indicate that chemical solution grown LMO is a promising perovskite building block for all-oxide multifunctional high-frequency spintronics devices.

Author contributions

The manuscript was written through contributions of all authors. All authors have given approval to the final version of the manuscript.

Conflicts of interest

There are no conflicts to declare.

Acknowledgements

We acknowledge financial support from the Spanish Ministry of Science, Innovation and Universities through Severo Ochoa (CEX2019-000917-S), and SPINCURIOX (RTI2018-099960-BI00) and AMONANO (PID2020-112914RB-I00) projects co-financed by the European Regional Development Funds. AMONANO also received funding from the European Union's Horizon 2020 research and innovation program under grant agreement no. 823717-ESTEEM3. Hailin Wang acknowledges financial support from the China Scholarship Council (CSC).

References

1 See chapters 1-3 In *Epitaxial growth of complex metal oxides*, ed. G. Koster, M. Huijben and G. Rijnders, Woodhead Publishing Series in Electronic and Optical Materials, Woodhead Publishing, 2015, ch. 1–3, pp. 1–68, ISBN 9781782422457.
2 J. E. ten Elshof, In *Chemical solution deposition techniques for epitaxial growth of complex oxides*, ed. G. Koster, M. Huijben and G. Rijnders, Woodhead Publishing Series in Electronic and Optical Materials. Epitaxial Growth of Complex Metal Oxides, Woodhead Publishing, 2015, ch. 4, pp. 69–93. ISBN 9781782422457.
3 Q. X. Jia, T. M. McCleskey, A. K. Burrell, Y. Lin, G. E. Collis, H. Wang, A. D. Li and S. R. Foltyn, *Nat. Mater.*, 2004, **3**, 529–532.
4 J. M. Vila-Fungueiriño, C. T. Bui, B. Rivas-Murias, E. Winkler, J. Milano, J. Santiso and F. Rivadulla, *J. Phys. D: Appl. Phys.*, 2016, **49**, 315001.
5 J. M. Vila-Fungueiriño, B. Rivas-Murias, J. Rubio-Zuazo, A. Carretero-Genevrier, M. Lazzari and F. Rivadulla, *J. Mater. Chem. C*, 2018, **6**, 3834.
6 H. Wang, J. Gazquez, C. Frontera, M. F. Chisholn, A. Pomar, B. Martinez and N. Mestres, *NPG Asia Mater.*, 2019, **11**, 41.
7 H. Wang, A. Pomar, S. Martin-Rio, C. Frontera, N. Mestres and B. Martinez, *J. Mater. Chem. C*, 2019, **7**, 12633.
8 A. Monsen, J. E. Boschkerb, F. Macià, J. W. Wells, P. Nordblad, A. D. Kent, R. Mathieu, T. Tybell and E. Wahlström, *J. Magn. Magn. Mater.*, 2014, **369**, 197–204.
9 A. Al Mamun, A. Haque, A. Pelton, B. Paul and K. Ghosh, *J. Magn. Magn. Mater.*, 2019, **478**, 132.
10 G. Y. Luo, C. R. Chang and J. G. Lin, *J. Appl. Phys.*, 2014, **115**, 17C508.
11 A. Hoffmann and S. D. Bader, *Phys. Rev. Appl.*, 2015, **4**, 047001.
12 L. Soumah, N. Beaulieu, L. Qassym, C. Carrétéro, E. Jacquet, R. Lebourgeois, J. Ben Youssef, P. Bortolotti, V. Cros and A. Anane, *Nat. Commun.*, 2018, **9**, 3355.
13 Q. Qin, S. He, W. Song, P. Yang, Q. Wu, Y. P. Feng and J. Chen, *Appl. Phys. Lett.*, 2017, **110**, 112401.
14 M. A. Schoen, D. Thonig, M. L. Schneider, T. J. Silva, H. T. Nembach, O. Eriksson, O. Karis and J. M. Shaw, *Nat. Phys.*, 2016, **12**, 839–842.
15 S. Crossley, A. G. Swartz, K. Nishio, Y. Hikita and H. Y. Hwang, *Phys. Rev. B*, 2019, **100**, 115163.

16 L. Liu, Q. Qin, W. Lin, C. Li, Q. Xie, S. He, X. Shu, C. Zhou, Z. Lim, J. Yu, W. Lu, M. Li, X. Yan, S. J. Pennycook and J. Chen, *Nat. Nanotechnol.*, 2019, **14**(10), 939–944.
17 M. Wahler, N. Homonnay, T. Richter, A. Müller, C. Eisenschmidt, B. Fuhrmann and G. Schmidt, *Sci. Rep.*, 2016, **6**, 28727.
18 S. Emori, U. S. Alaan, M. T. Gray, V. Sluka, Y. Chen, A. D. Kent and Y. Suzuki, *Phys. Rev. B*, 2016, **94**, 224423.
19 D. Castro Vaz, A. Barthélémy and M. Bibes, *Jpn. J. Appl. Phys.*, 2018, **57**, 0902A4.
20 J. Roqueta, A. Pomar, L. Balcells, C. Frontera, S. Valencia, R. Abrudan, B. Bozzo, Z. Konstantinovic, J. Santiso and B. Martinez, *Cryst. Growth Des.*, 2015, **15**, 5332–5337.
21 J. Töpfer and J. B. Goodenough, *J. Solid State Chem.*, 1997, **130**, 117–128.
22 M. Kareev, S. Prosandeev, J. Liu, C. Gan, A. Kareev, J. W. Freeland, M. Xiao and J. Chakhalian, *Appl. Phys. Lett.*, 2008, **93**, 061909.
23 M. Watanabe, E. Okunishi and K. Ishizuka, *Microsc. Anal.*, 2009, **23**, 5–7.
24 H. K. Schmid and W. Mader, *Micron*, 2006, **37**, 426.
25 P. Stamenov and J. M. D. Coey, *Rev. Sci. Instrum.*, 2006, **77**, 15106.
26 M. Farle, *Rep. Prog. Phys.*, 1998, **61**(7)), 755.
27 H. K. Lee, I. Barsukov, A. G. Swartz, B. Kim, L. Yang, H. Y. Hwang and I. N. Krivorotov, *AIP Adv.*, 2016, **6**, 055212.
28 Q. Qin, S. He, W. Song, P. Yang, Q. Wu, Y. P. Feng and J. Chen, *Appl. Phys. Lett.*, 2017, **110**, 112401.
29 C. Hauser, C. Ballani, P. Dürrenfeld, F. Heyroth, P. Trempler, S. G. Ebbinghaus, E. T. Papaioannou and G. Schmidt, *Phys. Status Solidi B*, 2020, **257**, 1900606.
30 R. A. Gallardo, A. Banholzer, K. Wagner, M. Körner, K. Lenz, M. Farle, J. Lindner, J. Fassbender and P. Landeros, *New J. Phys.*, 2014, **16**, 023015.
31 O. Mosendz, J. E. Pearson, F. Y. Fradin, G. E. W. Bauer, S. D. Bader and A. Hoffmann, *Phys. Rev. Lett.*, 2010, **104**, 046601.
32 H. Chen and D. Yi, *APL Mater.*, 2021, **9**, 060908.
33 J.-C. Rojas-Sánchez, *et al.*, *Phys. Rev. Lett.*, 2014, **112**(10)), 106602; J.-C. Rojas-Sánchez *et al.*, Spintronics VII, 2014. **Vol. 9167**, International Society for Optics and Photonics.
34 Xinde Tao, *et al.*, *Sci. Adv.*, 2018, **4**(6)), eaat1670.
35 Weifeng Zhang, *et al.*, *Nat. Phys.*, 2015, **11**(6)), 496–502.
36 M. Harder, G. Yongsheng and C.-M. Hu, *Phys. Rep.*, 2016, **661**, 1–59.
37 R. Mahendiran, *et al.*, *Phys. Rev. B: Condens. Matter Mater. Phys.*, 1996, **53**, 3348.
38 Y. Tserkovnyak, A. Brataas and G. Bauer, *Phys. Rev. Lett.*, 2002, **88**, 117601.
39 K. Harii, T. An, Y. Kajiwara, K. Ando, H. Nakayama, T. Yoshino and E. Saitoh, *J. Appl. Phys.*, 2011, **109**, 116105.
40 V. Castel, N. Vlietstra, B. J. van Wees and J. Ben Youssef, *Phys. Rev. B: Condens. Matter Mater. Phys.*, 2012, **86**, 134419.
41 Y. Wang, P. Deorani, X. Qiu, J. Hyun Kwon and H. Yang, *Appl. Phys. Lett.*, 2014, **105**, 152412.
42 M. Wahler, N. Homonnay and T. Richter, *et al.*, *Sci. Rep.*, 2016, **6**, 28727.
43 V. A. Atsarkin, I. V. Borisenko, V. V. Demidov and T. A. Shaikhulov, *J. Phys. D: Appl. Phys.*, 2018, **51**, 245002; V. A. Atsarkin, V. V. Demidov and T. A. Shaikhulov, *J. Exp. Theor. Phys.*, 2020, **130**, 228.
44 L. Vila, T. Kimura and Y. Otani, *Phys. Rev. Lett.*, 2007, **99**, 226604.
45 S. Meyer, M. Althammer, S. Geprägs, M. Opel, R. Gross and S. T. B. Goennenwein, *Appl. Phys. Lett.*, 2014, **104**, 242411.
46 M. Isasa, E. Villamor, L. E. Hueso, M. Gradhand and F. Casanova, *Phys. Rev. B: Condens. Matter Mater. Phys.*, 2015, **91**, 024402.
47 T. Kimura, T. Sato and Y. Otani, *Phys. Rev. Lett.*, 2008, **100**, 066602.
48 S. R. Marmion, M. Ali, M. McLaren, D. A. Williams and B. J. Hickey, *Phys. Rev. B: Condens. Matter Mater. Phys.*, 2014, **89**, 220404(R).
49 E. Shigematsu, *et al.*, *Appl. Phys. Express*, 2016, **9**, 053002.
50 R. Arias and D. L. Mills, *Phys. Rev. B: Condens. Matter Mater. Phys.*, 1999, **60**, 7395.
51 S. Azzawi, A. T. Hindmarch and D. Atkinson, *J. Phys. D: Appl. Phys.*, 2017, **50**, 473001.
52 V. Haspot, P. Noël, J.-P. Attané, L. Vila, M. Bibes, A. Anane and A. Barthélémy, *Phys. Rev. Mater.*, 2022, **6**, 024406.
53 V. Kambersky, *Czechoslovak J. Phys. B*, 1976, **26**, 1366.